Eulerian and Lagrangian Correspondence of High-Frequency Radar and Surface Drifter Data: Effects of Radar Resolution and Flow Components

I. I. Rʏᴘɪɴᴀ, A. R. Kɪʀɪɴᴄɪᴄʜ, R. Lɪᴍᴇʙᴜʀɴᴇʀ, ᴀɴᴅ I. A. Uᴅᴏᴠʏᴅᴄʜᴇɴᴋᴏᴠ

Woods Hole Oceanographic Institution, Woods Hole, Massachusetts

ABSTRACT

This study investigated the correspondence between the near-surface drifters from a mass drifter deployment near Martha's Vineyard, Massachusetts, and the surface current observations from a network of three high-resolution, high-frequency radars to understand the effects of the radar temporal and spatial resolution on the resulting Eulerian current velocities and Lagrangian trajectories and their predictability. The radar-based surface currents were found to be unbiased in direction but biased in magnitude with respect to drifter velocities. The radar systematically underestimated velocities by approximately $2 \, \text{cm s}^{-1}$ due to the smoothing effects of spatial and temporal averaging. The radar accuracy, quantified by the domain-averaged rms difference between instantaneous radar and drifter velocities, was found to be about $3.8 \, \text{cm s}^{-1}$. A Lagrangian comparison between the real and simulated drifters resulted in the separation distances of roughly 1 km over the course of 10 h, or an equivalent separation speed of approximately $2.8 \, \text{cm s}^{-1}$. The effects of the temporal and spatial radar resolution were examined by degrading the radar fields to coarser resolutions, revealing the existence of critical scales (1.5–2 km and 3 h) beyond which the ability of the radar to reproduce drifter trajectories decreased more rapidly. Finally, the importance of the different flow components present during the experiment—mean, tidal, locally wind-driven currents, and the residual velocities—was analyzed, finding that, during the study period, a combination of tidal, locally wind-driven, and mean currents were insufficient to reliably reproduce, with minimal degradation, the trajectories of real drifters. Instead, a minimum combination of the tidal and residual currents was required.

1. Introduction

High-frequency (HF) radar stations, now installed at numerous locations around the United States and the world, have been shown to provide useful estimates of surface currents in many current and wave environments (Paduan and Graber 1997; Kohut et al. 2004; Kosro 2005; Ramp et al. 2005). In the United States, the regional associations funded by National Oceanic and Atmospheric Administration (NOAA)'s Integrated Ocean Observing System (IOOS) office maintain more than 130 individual radars, all contributing data to a national network that provides estimates of surface currents over much of the coastal areas of the lower 48 states for a wide range of scientific and operational uses, including studies of across-shelf exchange, fisheries stock assessments, and search and rescue

operations, as well as pollution and harmful algal bloom tracking.

For operational users, short time prediction systems have been developed (O'Donnell et al. 2005; Barrick et al. 2012) to forecast near-term (0–12 h) surface currents based on recently observed HF radar currents. Utilizing relatively simple forecasting schemes, these systems were shown to cut predicted search areas in half and are in operational use by the U.S. Coast Guard. However, it was noted by O'Donnell et al. (2005) that reductions of the errors in HF radar–based trajectories and their uncertainty estimates would offer significant improvements to the short time prediction systems. Efforts by IOOS to track the surface plume during the Deepwater Horizon oil spill (IOOS 2011) further highlight the need for accurate trajectory products with known uncertainties.

Relative HF radar velocity errors, as rms differences with in situ observations, vary with the radar transmission frequency, sensor type, placement, and location within the sampled domain, as well as the data processing schemes used. Comparisons between HF radar

Corresponding author address: Irina Rypina, Physical Oceanography, MS #21, Woods Hole Oceanographic Institution, 266 Woods Hole Rd., Woods Hole, MA 02543-1050.
E-mail: irypina@whoi.edu

data and near-surface measurements of velocity using ADCPs suggest differences of 10–20 cm s^{-1} for long-range (4–5 MHz) systems with slightly reduced values of 7–10 cm s^{-1} for 11–13 or 24–26-MHz systems (Emery et al. 2004; Ullman and Codiga 2004; Kohut et al. 2006; Paduan et al. 2006). Several studies have directly compared HF radar data to near-surface drifter speeds or trajectories. Published drifter–radar velocity comparisons range from rms differences of 5–6 cm s^{-1} (Molcard et al. 2009; Ohlmann et al. 2007) to 27 cm s^{-1} (Barrick et al. 1977). Comparisons of Lagrangian drifter and pseudodrifter trajectories by Ullman et al. (2006) and Shadden et al. (2009) found separations of 5–10 km after 1 day of travel, or separation speeds of 6–11 cm s^{-1}. However, most comparisons have tracked drifters drogued at deeper depths than the effective depth of the radars and utilized radars with temporal and spatial resolutions of 3 h and 6 km, respectively, for 4–5 MHz systems (Ohlmann et al. 2007; Stewart and Joy 1974; Barrick et al. 1977) or 1 h and 1.5–3 km, respectively, for higher-frequency systems (Ullman et al. 2006; Shadden et al. 2009). Significantly smaller drifter and pseudodrifter separation rates of 2 km day^{-1} were recently reported by Molcard et al. (2009) using short-range very high-frequency (VHF) radars with resolutions of 600 m.

These prior studies suggest that the spatial and temporal resolution of the HF radar has a significant effect on the resulting velocities and trajectories, as well as their uncertainties. An opportunity to further explore these ideas was created by a pilot mass drifter release conducted in coastal waters near Martha's Vineyard, Massachusetts. While the goals of this pilot study were to test the performance of the drifters' advanced data acquisition systems as well as a unique vessel direction program for optimizing the drifter recovery, in preparation for future deployments to aid dynamical systems analysis of coastal circulation (Lekien et al. 2005; Shadden et al. 2009; Olascoaga et al. 2006), much of the drifter release occurred within the footprint of a new high-resolution, HF radar system, allowing for substantial radar–drifter intercomparisons. This study seeks to make use of this collocated dataset to perform a quantitative assessment of the Eulerian and Lagrangian correspondence between drifter velocities/ trajectories and the surface currents/pseudotrajectories derived from the HF radar system, to investigate the effects of the HF radar spatial and temporal resolution on the drifter–radar correspondence, and to document our abilities to predict surface trajectories based on linear models of the dominant components of the observed flows.

The paper is organized as follows: first, a description of the drifter release experiment, HF radar system, ancillary data, and regional oceanographic context is presented in section 2. In section 3, we present a detailed comparison of drifter- and radar-based velocities and trajectories and investigate the potential sources of the discrepancies. In section 4, we repeat these comparisons after deteriorating the radar resolution to quantify the effects of resolution on the accuracy of HF radar–based predictions. In section 5, we single out the various flow components from the HF radar velocity observations, including the mean, tidal, locally wind-driven, and "residual" currents, and investigate their relative importance for reproducing trajectories of real drifters. A summary of the results is then presented in section 6 along with conclusions regarding potential improvements to HF radar system performance.

2. Data and methods

a. Mass drifter release pilot study

In August 2011, a mass drifter experiment was conducted south of Martha's Vineyard, releasing large numbers of Coastal Ocean Dynamics Experiment (CODE)-type surface drifters in close proximity to the coast and partially within the footprint of the Martha's Vineyard HF radar system described next. During the experiment, 80 near-surface ClearSat drifters (http://clearwaterinstrumentation.com/products/clearsat-1/) were deployed inside a rectangular 8 km × 6 km domain, with approximate spacings of 700 m between neighboring drifters, and recovered 3 days later (Fig. 1). Fifty-three of the drifters were deployed within the HF radar footprint (Fig. 3). Drifter GPS positions were logged at 1-min intervals and transmitted onshore via Iridium-based text messaging every 5 min.

The experiment itself was a pilot study evaluating the ability of mass drifter releases to aid in the identification of Lagrangian coherent structures (LCSs), which are special material curves that delineate the flow into regions of qualitatively different Lagrangian motion (Haller 2002; Samelson and Wiggins 2006; Rypina et al. 2010). Specifically, the main goal of the experiment was to test, in real oceanic settings, a new technique from the dynamical systems theory, the so-called complexity measure method (Rypina et al. 2011), which allows identifying Lagrangian coherent structures directly from drifter trajectories. This goal dictated the size, shape, and location of the deployment domain, as well as the drifter deployment configuration and spacing, and position sampling frequency—all of which were optimized for identification of Lagrangian coherent structures. The complexity measure method is based on measuring the "complexity" of individual drifter trajectories by
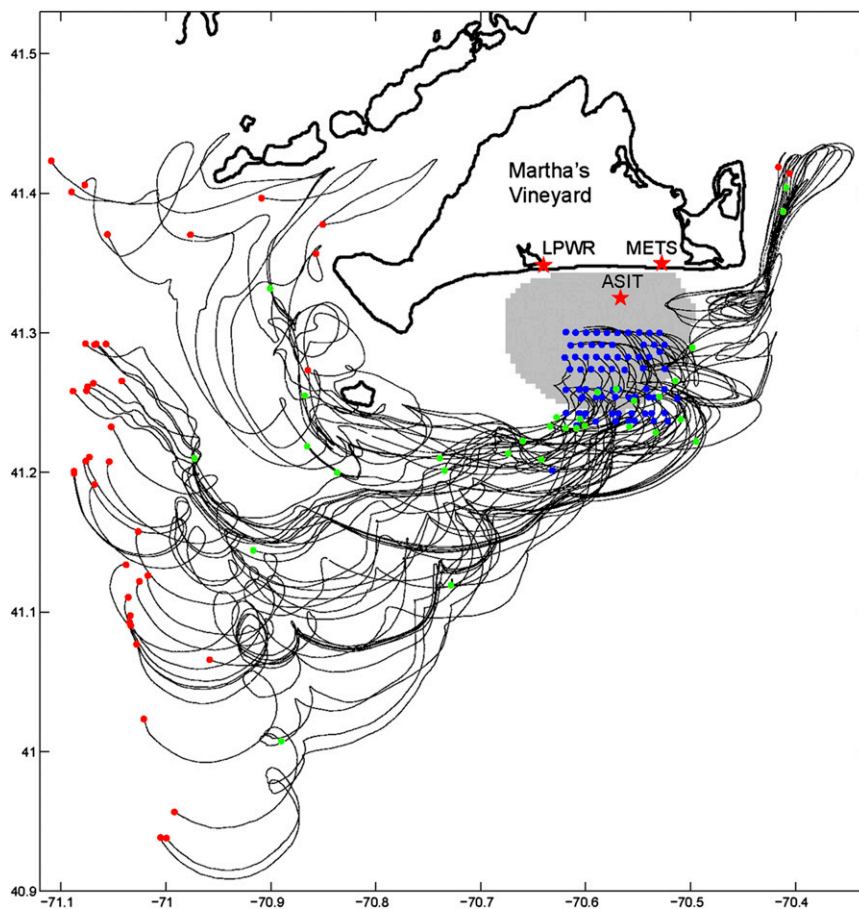
FIG. 1. Spaghetti plot of drifter trajectories from the drifter pilot study. First position fix for each trajectory is shown in blue and last position fix in green/red for faulty-/normal-performing drifters. Gray shaded area shows the HF radar footprint, red stars show positions of the three HF radar sites, and thick black curve indicates land.

computing their pathlengths, correlation dimensions, and ergodicity defects. The latter two characteristics quantify how well a trajectory samples space at different spatial scales and require high-frequency sampling rates (hence, the 1-min sampling). Also essential for mapping out Lagrangian coherent structures was the simultaneous deployment of all drifters rather than reseeding smaller subsets of drifters at different times. The deployment domain—a 8 km × 6 km region starting 5 km offshore—was chosen to be large enough to ensure that it covered some prominent submesoscale LCSs while still being small enough to be sampled adequately by 80 drifters. The experiment site was chosen to maximize the potential overlap with the LCSs rather than maximizing the overlap with the HF radar coverage domain. The deployment geometries—triangular grids—were chosen to simplify comparisons between the complexity measure method and finite-time Lyapunov exponent–based methods for LCSs identification, whose

application is most straightforward on a triangular deployment grid. Additional goals of this pilot study were to test the performance of the drifters' advanced data acquisition systems as well as a unique vessel direction program for optimizing the drifter recovery, in preparation for future mass drifter deployments in coastal ocean. Thus, while not optimized for the drifter–radar intercomparisons, the results of the mass drifter release provided a rich dataset to examine the accuracy of the HF radar system and its abilities to predict particle trajectories.

The ClearSat drifters used had similar design and technical specifications to the CODE drifter originally developed by Dr. Russ Davis of Scripps Institution of Oceanography (SIO) and thus had similar water-following capabilities. Drifters of the same type have been recently used by Chen et al. (2014) to investigate the circulation in the Red Sea (see also http://www.whoi.edu/science/PO/coastal/Redsea/). Wind conditions during

the release were moderate for summertime winds south of Martha's Vineyard with a mean wind of about $5 \, \text{m s}^{-1}$ to the east-northeast during the first day of the experiment. Recent estimates of the expected slip of Davis-style drifters, drogued in the upper 1 m, during light wind conditions are 1–$2 \, \text{cm s}^{-1}$ (Ohlmann et al. 2007; Poulain et al. 2009). During stronger winds, published slippage estimates are more variable, but generally increase to 1–$3 \, \text{cm s}^{-1}$ (Molcard et al. 2009; Poulain et al. 2009).

Deployments were made from two vessels over a period of 3 h to minimize the distortion of the deployment pattern. The vessels were moving in parallel with each other, each one deploying four rows of 10 drifters (i.e., 40 drifters total per vessel). The first (second) vessels deployed the four northernmost (southernmost) rows. During deployment both vessels were navigating in a zigzag pattern, starting from the northwestern corner of the corresponding deployment subdomain, first zigzagging eastward and seeding the two northernmost rows of drifters, and then shifting south and zigzagging westward, seeding the third and fourth rows. The time delay between the deployment of the first (westernmost drifters in the first and fifth rows) and last (westernmost drifters of the fourth and eighth rows) drifters is about 3 h. Drifter recovery, more challenging due to the spatial spread of the instruments, was significantly aided by the fully autonomous software package developed by the authors which, in real-time, informed each vessel of the location of the nearest drifters to it within an assigned recovery area. Spanning a combined area of $2000 \, \text{km}^2$, the 40 drifters still reporting at the end of the experiment (see below) and 22 additional nonworking units identified visually were recovered in 12 h (excluding transit time to the site) using this technique. Confirming the utility of pilot studies, the experiment revealed a flaw in the firmware of the drifters, which caused the combined GPS/Iridium antenna to lock into a GPS state that prevented it from transmitting its position and, consequently, led to communication failures of 50% of the units over the 78-h period (drifter decay is shown in Fig. 2). It is important to note, however, that this problem led to lost transmissions and fewer position fixes than anticipated, but not to erroneous position data.

b. The MVCO HF radar system

The Martha's Vineyard Coastal Observatory (MVCO), located along the south coast of the island of Martha's Vineyard (Fig. 1), supports a new HF radar system designed to map inner-shelf currents with the highest possible spatial resolution (Kirincich et al. 2012). Deployed in 2010, the system measures currents at scales approaching 400 m within a $20 \, \text{km} \times 20 \, \text{km}$ domain south of Martha's Vineyard (Fig. 1). Because of
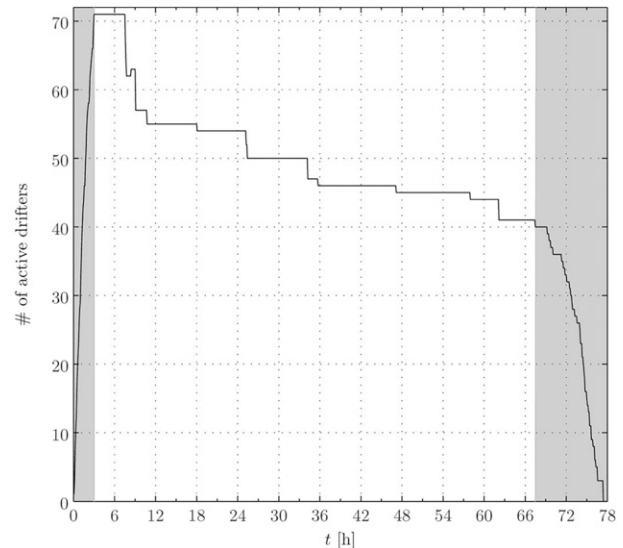

FIG. 2. Number of active drifters as a function of time. Deployment and recovery time intervals are marked by gray.

the system's spatial and temporal resolution as well as recent advances in HF radar data processing methods applied to the resulting dataset, as described below, this system is ideal for exploring the effects of environmental or instrument sampling with the goal of improving the accuracy of HF radar trajectory predictions. The system is composed of three closely spaced sites with SeaSonde-type direction-finding instruments running at operating frequencies near 25 MHz. During the study period, two of the three sites were located on land, with one placed at the MVCO Shore Meteorological Station (METS) and the second approximately 10 km to the west at the Long Point Wildlife Refuge. The third site was located on the MVCO Air–Sea Interaction Tower (ASIT), approximately 4 km offshore and south of the island. The effect of the tower site on the land sites, and vice versa, was carefully evaluated during the system setup, and potential interferences were mitigated using a combination of low transmit power, GPS-based timing offsets, sweep direction differences, and small offsets of the center frequencies for all sites. A full description of the system and the data processing techniques used are given in Kirincich et al. (2012, 2013); however, details pertinent to the work presented here are summarized below.

The deployment locations, operating bandwidth, and calibration procedures of the MVCO system were designed to achieve the maximum possible system resolution and accuracy. Because of the combination of site placement and an operating bandwidth of 350 kHz, the system was able to resolve currents at horizontal scales approaching 400 m starting about 700 m off of the coastline and extending out to 20 km with little
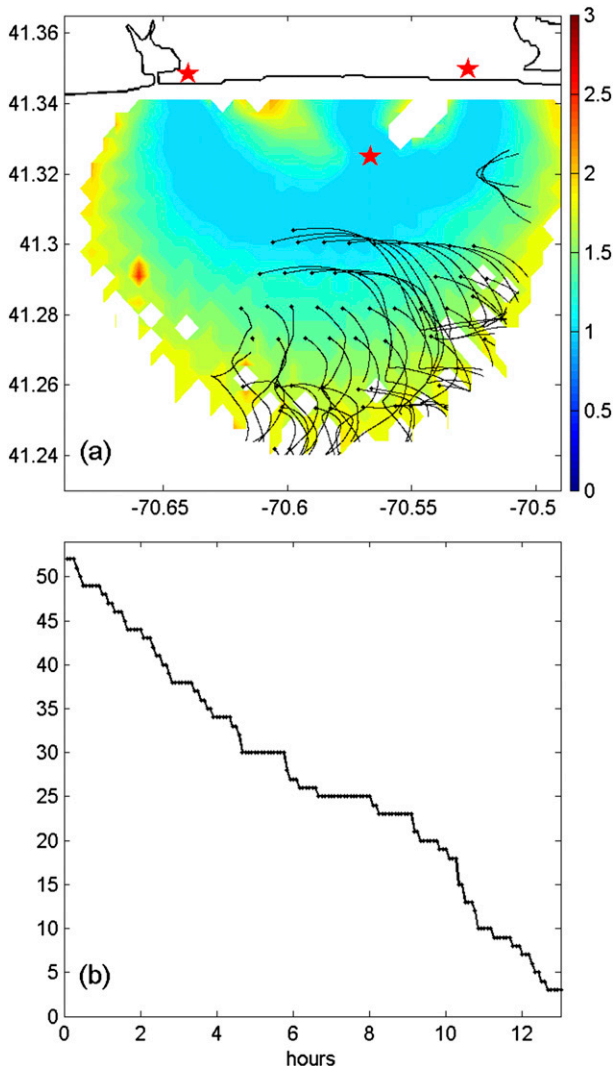
FIG. 3. (a) Segments of drifter tracks lying inside the HF radar footprint. Background color shows HF radar GDOP map. Red stars show locations of the three HF radar sites. (b) Number of drifters as a function of time spent by the drifter within the radar domain.

geometric dilution of precision (Fig. 3a). In comparison, most coastal, nonestuarine HF radar sites obtain radial spatial resolutions of 2–8 km out to ranges of approximately 45–130 km, depending on the operating frequency. For the MVCO systems, the response pattern of each antenna system was carefully calibrated twice per year, including an iterative analysis of the spatial structure of observed tidal ellipses in order to minimize time-invariant bearing-related errors (Kirincich et al. 2012).

To maximize the spatial and temporal independence of the observations as well as the velocity resolution of the system, spectral estimates of the observed Doppler-shifted radial velocities (Crombie 1955; Barrick et al. 1977; Paduan and Graber 1997) were collected in bursts of 1024 nonoverlapping frequency sweeps with a sweep

rate of 2 Hz for finer velocity resolution of Doppler velocities (~1.2 cm s^{-1}) than is typical for 25-MHz systems without interpolation. A maximum of three, but normally two, successive spectral estimates were averaged to create an ensemble spectral estimate every 15 min. Direction-finding (Schmidt 1986; Barrick and Lipa 1997) and azimuthal averaging into 5° bands was performed on each ensemble average using a backscatter power-weighted method, described by Kirincich et al. (2012), that was shown to decrease rms differences against ADCP near-surface velocities by up to 2–3 cm s^{-1}. No interpolation was used to smooth the fields or fill in radial gaps, but as in previous works, outliers were removed before computing vector velocities.

During the period of the drifter experiment, vector velocities were estimated within the shaded area in Fig. 1 every 0.5 h for each point on a regularly spaced grid with 400-m horizontal resolution from all available radials within an averaging radius of 400 m and a time window of 0.5 h. However, it should be noted that although the nominal spatial resolution of the radial velocities varied from 400 to 800 m throughout the domain due to the use of azimuthal bins, the vector averaging described here essentially smoothed out all features on scales less than 800 m. Following the work of Stewart and Joy (1974), surface velocities obtained by the 25-MHz radar system have an effective depth of 0.5 m compared with the 1-m-depth-averaged measurements from the drifters. As described by Ullman et al. (2006) and Ohlmann et al. (2007), this difference is not likely to cause a substantial part of discrepancies between the two, except for instances of high wind-driven near-surface shears.

c. Meteorological observations

Measurements of wind velocity were made by MVCO at two locations—the METS and ASIT stations. The wind record at ASIT is believed to be most representative of the winds present over the study area and was used here to compute wind stress during the summer period (June–September). Wind stress was estimated following the bulk formula of Large and Pond (1981).

d. Regional oceanographic context

The inner shelf south of Martha's Vineyard has been the site of numerous studies on coastal circulation and atmospheric boundary layers (Edson et al. 2007; Gerbi et al. 2008; He and Wilkin 2006; Wilkin 2006). MVCO has been in place for more than 10 years. Generally, the area is thought to be an extension of the southern New England shelf, subject to wind-driven coastal upwelling or downwelling, and bouyancy-driven flows resulting from the strong tidal mixing occurring on the nearby Nantucket Shoals, superimposed on a mean southward

drift (Shearman and Lentz 2004; Wilkin 2006; Lentz 2008).

Specific to work on the inner shelf, the study area has been the site of work exploring new mechanisms of across-shelf exchange as well as the effects of spatially variable mean and tidal circulations. Fewings et al. (2008) and Lentz et al. (2008) recently documented the roles of across-shelf winds and wave forcing on the depth-dependent across-shelf circulation present, finding that across-shelf winds drove most of the upwelling circulation at water depths less than 15 m. Additionally, high-resolution model output for the region (Ganju et al. 2011) and initial observations from the MVCO HF radar system (Kirincich et al. 2013) have documented significant spatial variability of the depth-independent tidal and mean circulation, which has the potential to drive significant lateral exchange across the inner shelf. Thus, the relative importance of the different circulation components—that is, mean, tidal, or wind driven—is of interest toward understanding the dynamics present in this coastal environment as well as their predictability.

3. Drifter-to-radar intercomparison

Figure 3 shows segments of drifter tracks lying within the footprint of the radar, from the time of deployment until the drifters leave the radar domain or stop transmitting. Initially, 53 drifters were deployed inside the domain, but 3 of these drifters stopped transmitting while within the domain and the rest flowed out of the domain, so the total number of drifters within the domain decreased with time as shown in Fig. 3b. The total number of position fixes inside the radar footprint was over 2×10^4. The standard deviation (STD) of GPS positioning error in the region was ~3 m, based on tests done at Woods Hole Oceanographic Institution (WHOI) and by the manufacturer. The time delay between the deployment of the first and last drifters was about 3 h, so the differences between individual drifter tracks were due to both spatial and temporal variability of the underlying velocity field. Specifically, the divergence of trajectories near {41.285, −70.61}, with the northward-moving tracks north of 41.285°N and southward-moving tracks south of 41.285°N, was mainly due to the temporal changes of the flow field during the 3-h-long deployment rather than due to the spatial variability of the velocity field.

a. Eulerian comparison between the drifter- and radar-based velocities

The drifter positions can be converted to velocities and then compared to the corresponding radar-based estimates interpolated to the time and location of the drifter. Drifter- and radar-based velocity estimates should be in general agreement with each other; however, the two estimates are not expected to be identical due to the GPS positioning error (3 m), different effective depths of the velocity measurements (0.5 m for radar and 1 m for drifters), drifter slippage (1–3 cm s^{-1}), and the radar-induced smoothing and interpolation. While the drifters provide instantaneous position fixes, the radar measures spatially and temporally averaged currents as described above. In our analysis, we applied a 30-min running average to the 1-min position fixes along each drifter trajectory before converting positions to velocities. This was done to effectively decrease the GPS positioning errors, increase the signal-to-noise ratio of the positioning estimates, and produce more reliable estimates of drifter velocities. The 30-min window for the running average was chosen as a compromise between accuracy and resolution. Longer averaging would improve accuracy but decrease resolution and vice versa. Our reasoning for the 30-min window was to keep the averaging time sufficiently short compared to the velocity decorrelation time (about 3 h) in order to retain the important temporal variability of the signal, but at the same time to keep it long enough to significantly improve the signal-to-noise ratio of the drifter positions. An additional advantage of using the 30-min averaging is that the resulting drifter velocities are "most consistent" with the radar estimates, which use the same averaging time. It is important to keep in mind, however, that although the averaging times are the same, the along-trajectory drifter position smoothing (i.e., average along a one-dimensional curve) is different from the radar velocity smoothing, which is performed within the radial spatial cells (i.e., average over a two-dimensional area).

Figure 4 quantifies the comparison between the drifter velocities and radar-based velocities interpolated to the drifter positions using a bilinear interpolation in space and time. We have carefully checked that our results are insensitive to the interpolation method used, and we only list these details for completeness. Figure 4a shows the two estimates plotted on top of each other using arrows of different colors. A more quantitative analysis is presented in the middle and bottom panels. Figures 4b and 4c show scatterplots of the drifter versus radar velocity estimates in the zonal (u, left) and meridional (v, right) directions. In both directions, the drifter and radar velocities agreed closely on average, with the mean and STD values for the velocity differences of 1.2 ± 4.2 cm s^{-1} for the zonal and −1.2 ± 2.3 cm s^{-1} for the meridional components. The correlation coefficient between the drifter and radar estimates was 0.94 for the zonal and 0.95 for the meridional velocity components.
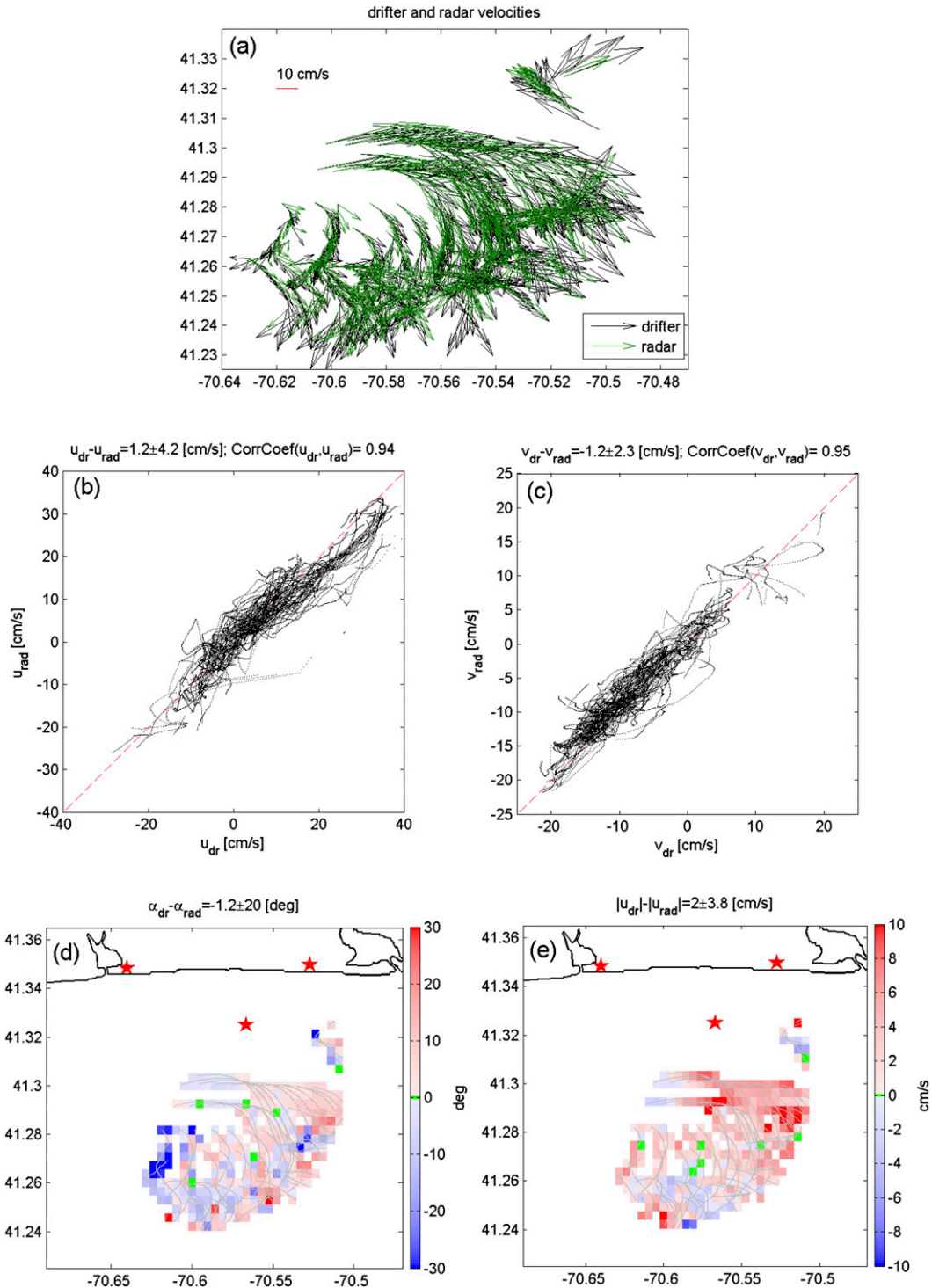
FIG. 4. (a) Drifter-based (green) and radar-based (black) velocity estimates. (b),(c) Scatterplot of drifter (u_{dr}, v_{dr}) vs radar-based (u_{rad}, v_{rad}) velocities in (b) zonal and (c) meridional directions. Corresponding correlation coefficients are listed above the subplots. Red dashed line is a diagonal. Difference in (d) direction and (e) magnitude between the drifter- and radar-based velocities. Domain-averaged mean and STD differences are listed above each of the bottom panels. Red stars show locations of the three HF radar sites.

We have also carried out the comparisons between collocated radial velocities measured by each of the three radar stations, estimated every 15 min, and drifter velocities rotated into the corresponding "radial" coordinate system. The resulting domain-averaged mean (rms) differences between drifter and radar radial velocities were from -4 to -1 (from 6 to 10) cm s^{-1}, depending on the radar site, with correlation coefficients greater than 0.83 for all three sites. The rms differences in "raw" radial velocities were larger than for the "processed" zonal and meridional components because each processed estimate made use of several raw radials, which led to a significant noise reduction in radar velocity estimates. The obtained radial drifter-to-radar rms differences were slightly higher than the estimate of 5 cm s^{-1} reported by Molcard et al. (2009) and were similar to the radar and near-surface ADCP comparisons reported by Kirincich et al. (2012).

The spatial distribution of the radar velocity errors in both direction and magnitude were estimated by computing the mean difference in direction (Fig. 4d) and magnitude (Fig. 4e) between the drifter- and radar-based velocities for each 400 m × 400 m box. The spatial patterns shown are different from, and cannot be directly explained by, the radar geometric dilution of precision (GDOP) map (Fig. 3a). Direction differences vary throughout the domain. Radar velocities tend to point to the left (right) from the drifter-based velocities estimated in the western (eastern) part of the domain. The blue region of the largest negative differences in direction located in the southwestern corner of Fig. 4d is characterized by small velocity magnitudes and potentially related to the increased susceptibility of directional errors for very weak currents. However, looking at the spatial structure of either the direction or velocity differences is somewhat confounded by the variable temporal sampling within each box. For example, the differences in velocity magnitudes in Fig. 4e are largest in the northeastern corner of the domain. However, drifters occupied this area for a short period during a strong nearly zonal flow ($u_{dr} > 20$ cm s^{-1}), suggesting that the differences seen could be specific to this particular flow event rather than to this geographical area in general.

The domain-averaged mean and STD of the direction and magnitude differences are given in Figs. 4d and 4e, respectively. The former could be interpreted as the domain-averaged radar bias, and the latter provides an estimate for the STD radar velocity error compared to drifters. Our analysis suggests that, on average, radar velocity estimates were essentially unbiased in direction, as the mean bias of 1.2° was not statistically significant but that the radar systematically underestimated the velocity magnitudes by 2 cm s^{-1} compared to drifters. As

described above, although the same averaging time of 30 min was used for both drifter and radar datasets, the radar data were subject to a larger amount of spatial smoothing than the drifter data. For this reason, it is expected that the radar smoothing would be more effective in removing the extreme values, leading to the slightly smaller radar velocity magnitudes compared to the drifter estimates. Supporting this explanation, a comparison between the same smoothed radar velocity data and unsmoothed drifter data (without the 30-min running average) led to a slightly ($\sim$10%) larger underestimate in the radar velocity magnitude compared to drifter velocity magnitude. The overall STD of the differences between the radar and drifter velocities was about 3.8 cm s^{-1}, which is slightly less than the approximately 4.7–5 cm s^{-1} rms differences found between near-surface ADCP observations from the MVCO 12-m underwater node (Kirincich et al. 2012) and the overlying radar-based surface currents for the full summer. When reconciling these numbers, however, it is important to keep in mind the inequality between the ADCP–radar velocity differences at the ADCP location and over a full season, and the domain-averaged drifter–radar velocity differences over the 3-day period of this experiment.

b. Lagrangian comparison between the real and simulated trajectories

In the previous section, we quantified Eulerian differences in velocities between the drifters and the radar. However, these velocity differences can cancel or reinforce each other along a Lagrangian trajectory as it winds through different geographical regions. Thus, converting these velocity differences directly into separations between real and radar-based simulated drifters is not straightforward. To investigate the ability of the radar to reproduce trajectories of real drifters, we carried out a Lagrangian analysis in which the velocity estimates from the HF radar were integrated to produce simulated trajectories (Fig. 5), which were then compared to trajectories of real drifters within the domain. As before, a 30-min running average was applied to the 1-min position fixes along each drifter trajectory before comparing them to the radar-based simulated trajectories. To compute trajectories from the HF radar velocities, we used a variable-step fourth-order Runge–Kutta trajectory integration scheme [RK4(5) in (MATLAB)] with bilinear velocity interpolation in space and time.

Overall, the shape and extent of the simulated trajectories matched that for the real drifters, but the details (i.e., exact positions of the small-scale wiggles, loops, and cusps) of the two were different. As a result, simulated trajectories diverged from the real ones with time. This separation between the real and simulated
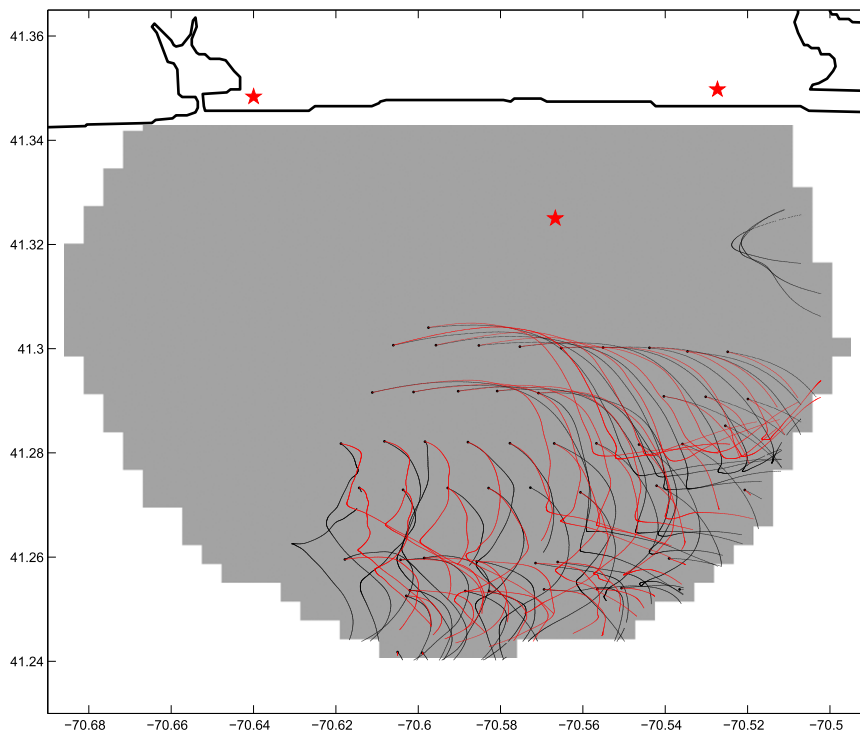
FIG. 5. Real (black) and simulated (red) drifter trajectories estimated from the HF radar velocities. Red stars show locations of the three HF radar sites.

trajectory pairs over time can be used to quantify the ability of the radar to reproduce the Lagrangian drifter trajectories.

To increase the number of available real/simulated trajectory pairs and to improve the statistics of our estimates, we divided drifter trajectories into independent segments and seeded simulated drifters at the beginning of each independent segment (rather than just at the beginning of each trajectory). The segments were considered to be independent if the detided velocity decorrelated from one segment to the next—that is, if the corresponding Lagrangian velocity autocorrelation function fell below its *e*-folding value. Figure 6 shows the individual (gray) and mean (red) Lagrangian autocorrelation functions for the detided drifter velocities in the zonal and meridional directions. The decorrelation time scale, defined as the *e*-folding time of the velocity autocorrelation function, was found to be 3.2 and 2.7 h for the zonal and meridional velocity components, respectively. So, roughly speaking, we reseeded simulated drifters every 3 h along each trajectory. The decorrelation time of several hours found for the Martha's Vineyard inner shelf is much shorter than that for the open ocean, which is on the order of several days, as estimated by Lumpkin et al. (2002); this points to the importance of small-scale features in governing the evolution and spread of passive tracers in the coastal ocean.

The resulting ensemble-averaged separation between the real and simulated drifters as a function of time, along with the corresponding 1-STD confidence interval, is shown in Fig. 7a, while Fig. 7b indicates the number of the available independent real/simulated trajectory pairs that stayed within the radar domain over time intervals longer than *t*. The curve starts with 99 pairs but drops to fewer than 20 available pairs for $t >$ 9 h, leading to more noisy and less reliable estimates at longer times. In the mean, real and simulated drifters diverged from each other by 1 km in 10 h (Fig. 7a), yielding an average separation speed of $2.8 \, \text{cm s}^{-1}$. This estimate is in good agreement with Molcard et al. (2009), who reported separations of 1 km in 12 h between the real drifters and the radar-based pseudotrajectories in the Gulf of La Spezia [that study used a 45-MHz VHF Wellen Radar (WERA) with the 600-m processed or effective range resolution].

It is tempting to speculate on the underlying physical mechanisms leading to the observed separation between the real and simulated drifter pairs. The Eulerian analysis in the previous subsection revealed the existence of the mean bias (underestimate) in the radar velocity estimates as well as the rms differences between the drifter- and radar-based velocities. These two sources of error are expected to lead to different separation mechanisms between the real and simulated trajectory pairs.
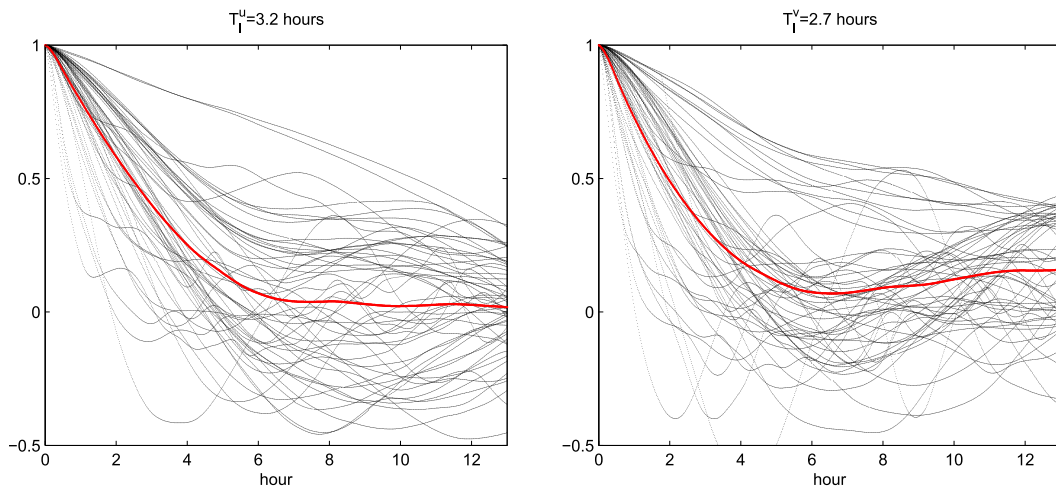
FIG. 6. Drifter-based Lagrangian velocity autocorrelation function in the (left) zonal and (right) meridional directions. Individual drifter estimates are shown in black, and mean is shown in red. Lagrangian decorrelation time scale, defined here as an *e*-folding time of the autocorrelation function, is shown above each panel.

The mean velocity underestimate is expected to cause ballistic spreading, so the corresponding separation should grow linearly with time, at least over short time scales when real and simulated drifters are still close to each other and their velocities are correlated. The random rms errors are expected to cause diffusive spreading, so the separation distance should be $\propto \sqrt{t}$. The cumulative separation is then expected to be a superposition of these two processes, with the square root dependence dominating at short times and the linear growth dominating at later times. Looking at the separation curve in Fig. 7a, one could speculate that this is indeed the observed behavior, with the transition from the square root to the linear process happening around 6 h. However, such argument should be applied with caution because it assumed that the velocity underestimation is spatially uniform and time independent, and that the rms errors are simply random. It is also important to keep in mind that the distance of 1 km is smaller than the characteristic length scale of the underlying velocity field, so real and simulated drifters in each pair are still correlated over the course of 10–12 h. Finally, we suggest that it might be possible to correct for the mean bias in the radar velocity estimates by simply increasing the radar velocity magnitudes by $2\,\mathrm{cm\,s}^{-1}$ while keeping the velocity directions unchanged. The resulting separation between the real and simulated drifter pairs (gray curve in Fig. 7a) slowed down when the bias was eliminated and the corresponding separation speed decreased from 2.8 to $2.3\,\mathrm{cm\,s}^{-1}$. One could also speculate that, consistent with the arguments made above, the gray curve more closely resembles the square root dependence than the black curve.

4. Effects of the radar resolution

As demonstrated above, the ability of the HF radar to reproduce real drifter trajectories depends on the spatial and temporal resolution of the radar velocity fields. While we cannot improve the radar product beyond the half-hour temporal and 400-m spatial resolution of the current radar settings, we can artificially degrade the radar resolution in both time and space to see how the agreement with drifters will change in response.

a. Spatial resolution

The spatial resolution was varied from 400 to 3600 m by convolving the radar velocity fields with a square window of the corresponding size. This is equivalent to averaging together $n = 1, \ldots, 8$ neighboring velocity vectors along the longitude and latitude directions. The resulting deteriorated velocity fields can then be interpolated to the drifter positions and times, and the Eulerian comparison can be performed as in section 3a. Figure 8 quantifies the agreement with drifters as a function of the radar spatial resolution. Degrading the spatial resolution does not introduce any significant bias in velocity direction (Fig. 8a) but leads to the consistently increasing underestimation of the velocity magnitude compared to the drifter-based velocities (Fig. 8b). This increase is due to the increasing size of the running-average (or convolution) procedure described above, which effectively eliminates the peak velocity values from the radar fields and results in the larger underestimation of the near-local drifter-based velocities. Although the difference with drifters increases monotonically with the degrading resolution, the rate of this
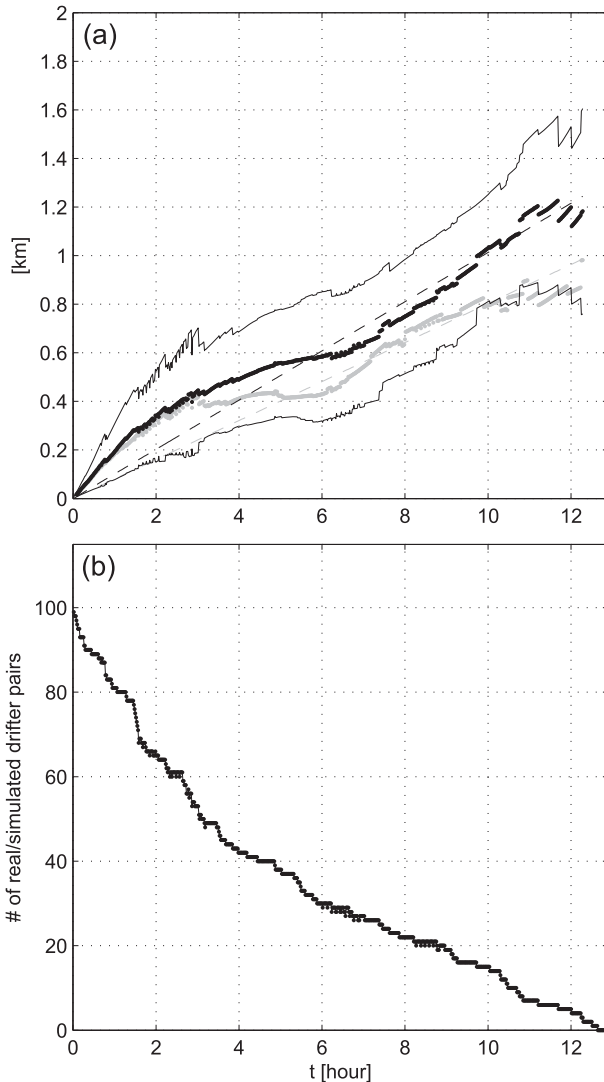
FIG. 7. (a) Black curves show ensemble-averaged separation between the real and simulated drifters, along with the corresponding 1-STD confidence interval, as a function of time. Black dashed line is the best linear fit of the form $D = v_{sep}t$ to data. Gray is the same as black but for the radar fields adjusted to account for the mean velocity bias. (b) Number of available real/simulated trajectory pairs that stay within the radar domain over time interval of t hours. Simulated drifters are seeded at the beginning of each independent trajectory segment.

increase is not uniform. Up until approximately 1200 m, the agreement between the drifter and radar velocity magnitudes is not very sensitive to the radar resolution, but it starts to deteriorate more rapidly from 1600 m and up.

The Lagrangian comparison of separation between the real and simulated drifter trajectories computed using the deteriorated radar velocities is shown in Fig. 9 out to times of 7 h. Similar to the Eulerian comparison, the separation between the real and pseudotrajectories generally increases, and thus the ability of the radar to

reproduce drifter tracks generally decreases as the radar resolution degrades. However, it is important to note that degrading the radar resolution by averaging neighboring grid points together leads to a decrease in the effective domain size, so trajectories leave the radar domain sooner than in the undeteriorated case. Because of this, the number of available real/simulated drifter pairs is different for different subplots. In particular, for the 400- (3600)-m resolution fields, there are 99 (34) pairs available at short times and only 25 (3) pairs at 7 h. Because of this reduction in sample size for the deteriorated cases, the comparisons are only shown for times up to 7 h. As explained above, the differences between the deteriorated (thick black) and undeteriorated (dashed) separation curves in each subplot are due to a combination of two factors: the effect of the resolution and the effect of the decreased domain size. We can quantify the relative importance of the second effect by recalculating the separation curve for the undeteriorated radar field but using only those trajectories that lie within the 3600-m-resolution domain. The result is shown in the bottom-right subplot of Fig. 9 by the dashed–dotted curve (which lies between the thick black and dashed curves). Comparison between the three curves suggests that the domain size effect accounts for roughly one-third of the difference between the deteriorated and undeteriorated curves, while the radar resolution accounts for the remaining two-thirds of the difference. Note also that, in spite of the degraded resolution, the growth of the initial segment of the separation curve over the first 3 h is slightly lower for the deteriorated fields than for the 400-m-resolution case. Additional analysis suggests that this difference is mostly due to the exclusion of trajectory segments lying near the perimeter of the domain, where the radar velocity errors are the largest, from the deteriorated separation curve.

To better quantify the comparisons shown in Fig. 9, we estimated the mean separation velocity between the real and simulated drifters in each comparison by fitting a line of the form $D = v_{sep}t$ to the separation curve (Fig. 10). Not surprisingly, the ability of the radar to reproduce the Lagrangian drifter trajectories generally decreases and, consequently, the separation velocity generally increases (apart from a small increase between the 400- and 800-m cases), with the degrading spatial resolution of the radar velocity field. Similar to the Eulerian comparison in Fig. 8, the separation velocity in Fig. 10 increases more rapidly when larger spatial scales (from 1600 m and over) become unresolved. The critical spatial resolution of about 1.5–2 km appears to be an intrinsic scale of the underlying fluid flow and not a function of the radar processing used. As shown here, not resolving
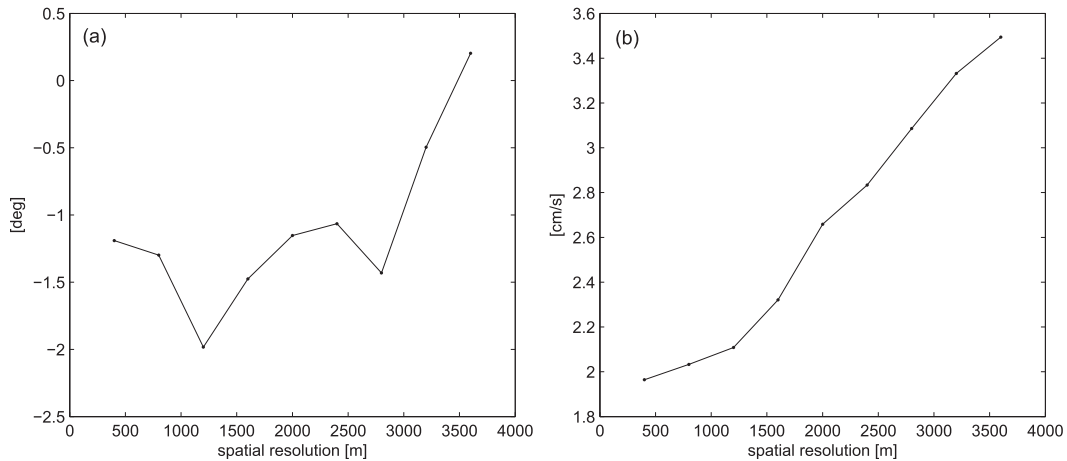
FIG. 8. The domain-averaged mean differences in (a) direction and (b) magnitude between the drifter- and radar-based Eularian velocities as a function of the radar spatial resolution.

this spatial resolution leads to significant increases in trajectory errors.

The insensitivity of the results to the change in the radar resolution from 400 to 800 m is likely because 400-m scales are underresolved even in the undeteriorated radar fields. As described above, although the nominal resolution of the gridded radar product is 400 m, the minimum spatial scales resolvable will be larger farther from the radar sites, up to a maximum of 800 m, due to both the averaging radius used to compute the vector velocities and the azimuthal averaging used to derive the radial velocities themselves. Azimuthal averaging is largest near the southern edge of the radar footprint, where a 5° averaging band is equivalent to 800–900 m, hence the small changes between the 400- and 800-m cases in Figs. 8–10.

b. Temporal resolution

We now turn our attention to investigating the effects of the temporal resolution. The temporal resolution of the radar was varied from 0.5 to 12 h by averaging together $n = 1, \ldots, 24$ consecutive time fixes of velocity at each grid point. As in the previous section, the resulting velocities were then interpolated to the drifter positions and times, and the Eulerian comparison between the drifter- and radar-based velocities as a function of the radar temporal resolution was performed. Agreement with drifters for both the radar-based velocity direction and velocity magnitude decreases steadily with degraded temporal resolution (Fig. 11), with mean velocity differences increasing from $2 \, \text{cm s}^{-1}$ at 0.5 h temporal resolution to $3 \, \text{cm s}^{-1}$ at 3 h and $6 \, \text{cm s}^{-1}$ at 10 h (Fig. 11b).

The sensitivity of the results—the change in slope as a function of radar resolution—is less pronounced and more difficult to interpret in Fig. 11b. Although the

difference in direction in Fig. 11a indicates a slope change at around 4 h (with weaker sensitivity to resolution changes between $dt = 0.5$ and 4 h and greater sensitivity afterward), the slope of the curve in Fig. 11b changes twice, around approximately 2 and 9 h, indicating weaker sensitivity to short and long temporal scales and stronger sensitivity to the intermediate temporal scales ($2 < t < 9$ h).

In contrast, a Lagrangian comparison between the real and simulated drifters (Figs. 12 and 13) found that separation velocities increases slowly between resolutions of 0.5 and approximately 3 h, before increasing more rapidly at longer time scales. The critical temporal scale of 3 h is possibly due to the important role tidal velocities play in the region. The semidiurnal, ~12-h tidal components dominate velocity variability in the region; thus, at greater than 3-h time steps—that is, with fewer than four points per period—the ability of the radar to adequately reproduce tidal motions is degraded and the simulated drifters diverge much faster from the real drifters. It is possible, however, that flow components other than tides exhibit temporal variability on similar scales. Interpreting the critical scale of about 3 h as an indication of the dominant role played by the tidal motions on the resulting motion of drifters might thus be deceptive. In the next section, we investigate the relative importance of different flow components in more detail.

5. Relative importance of different flow components during the study period

The total velocity field measured by the HF radar can be decomposed into different flow components based on the dominant forcing mechanisms potentially present: tidal motions, locally forced wind-driven events, and
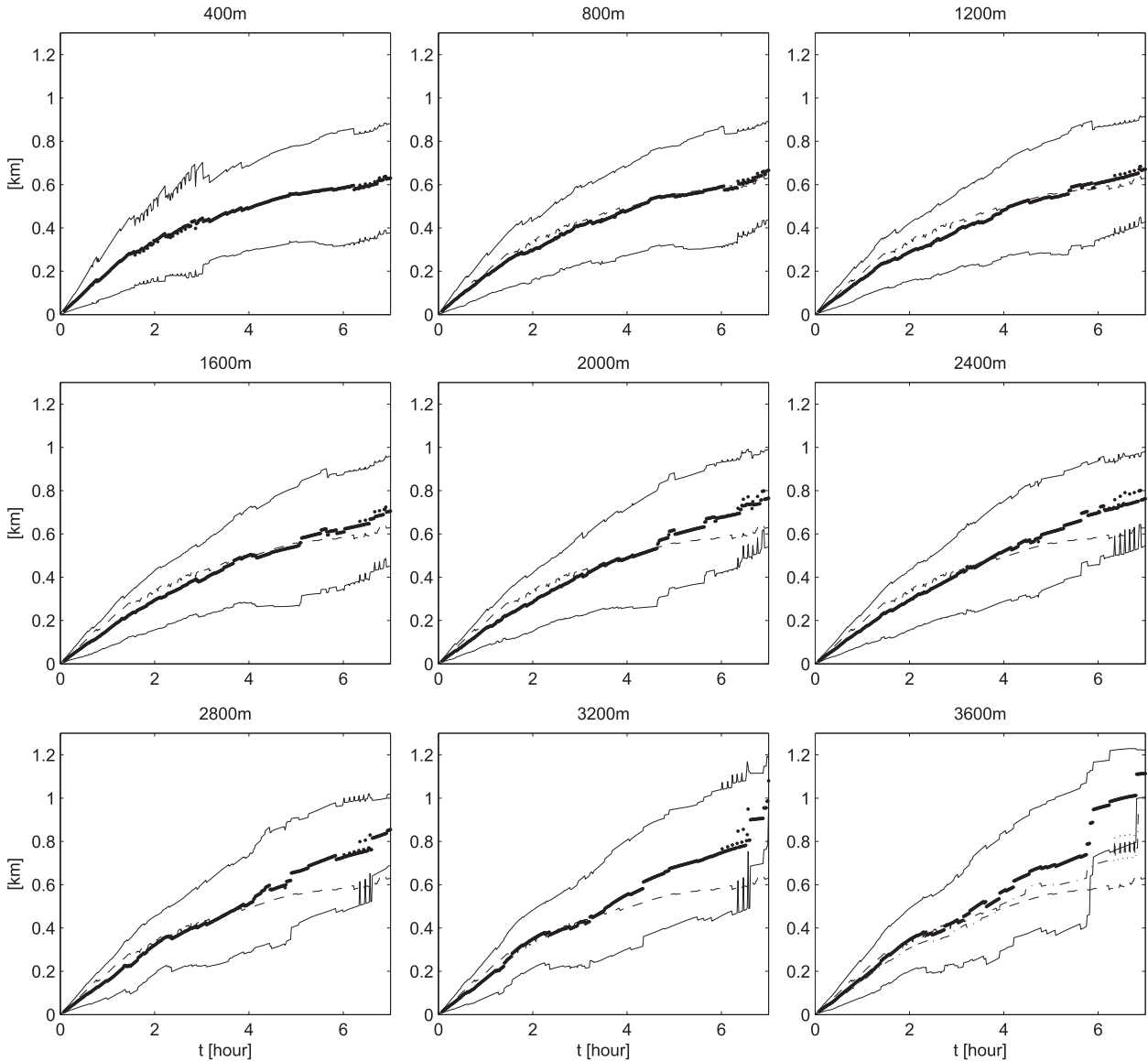
FIG. 9. As in Fig. 7, but for the deteriorated radar velocity fields with various resolutions from 400 m (undeteriorated resolution) to 3.6 km. To aid the comparison, the 400-m-resolution curve is shown as a dashed line in all panels. A second version of the 400-m curve, computed using only those trajectories that lie within the 3600-m domain, is shown as a dashed–dotted line in the bottom-right subplot.

a steady mean summer circulation pattern (Kirincich et al. 2013), as well as the remaining residual velocity variability. In the analysis that follows, the tidal currents present in the HF radar velocities for each grid location over the summer months were estimated using T_tide (Pawlowicz et al. 2002). The portion of the total velocity that could be related to the local wind forcing was estimated by calculating linear regression coefficients between the local winds measured at the ASIT tower, and the de-meaned and de-tided radar velocities during the summer period. These linear regressions were estimated separately for each grid location, by regressing each

component of the surface current on both the north and east components of the wind velocity, yielding four coefficients for each grid location. Local wind-driven velocities were then constructed by multiplying the resulting regression coefficients by the ASIT tower wind velocities at the time of the pilot study as

$$
\begin{bmatrix} u_{\text{wind-driven}}(x,y,t) \\ v_{\text{wind-driven}}(x,y,t) \end{bmatrix} = \begin{bmatrix} R_{11}(x,y) & R_{12}(x,y) \\ R_{21}(x,y) & R_{22}(x,y) \end{bmatrix} \times \begin{bmatrix} u_{\text{wind}}(t) \\ v_{\text{wind}}(t) \end{bmatrix}, \tag{1}
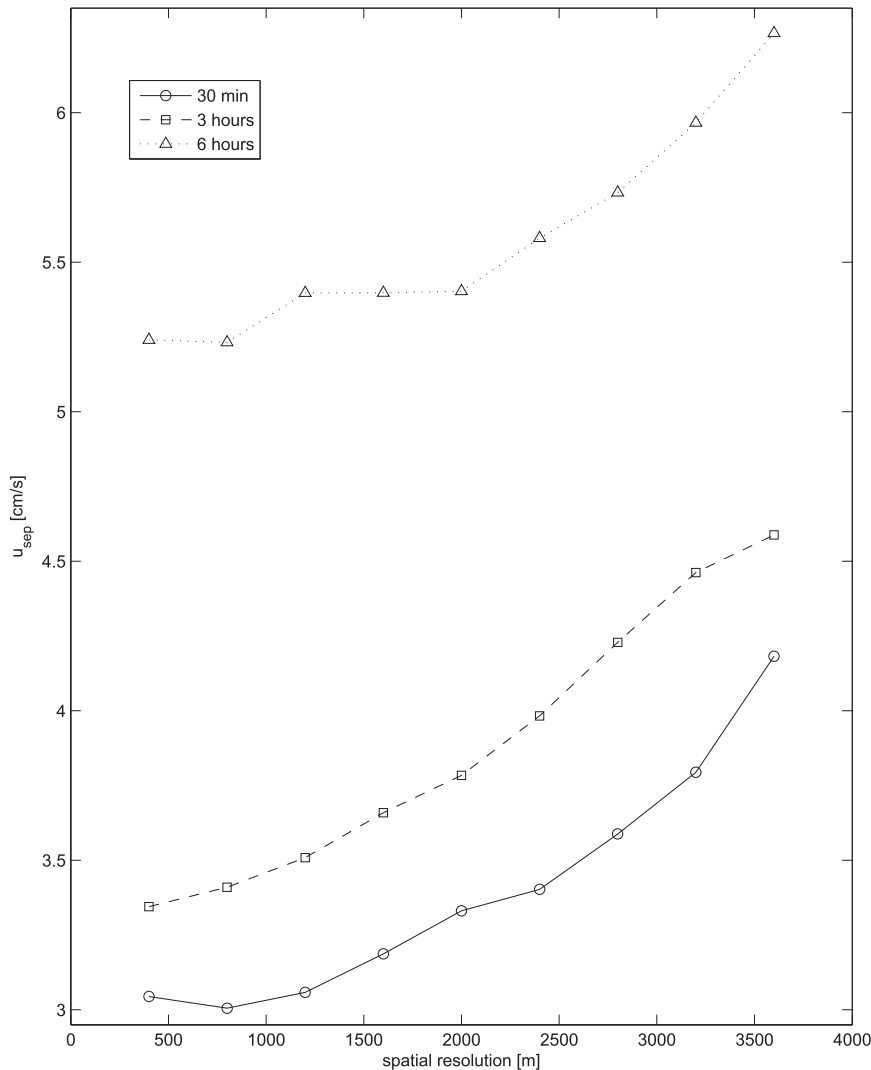$$

FIG. 10. Separation velocity, averaged over the first 7 h, between the real and simulated drifters as a function of the radar spatial resolution (solid curve). Dashed and dotted curves show the same result for radar fields temporally degraded to 3 and 6 h, respectively.

where $R_{ij}(x, y)$ with $i, j = 1, 2$ are the spatially dependent linear regression coefficients. The residual velocities were defined here as a difference between the total currents minus the mean, tidal, and locally wind-driven flows. They include velocity variability due to undefined dynamics such as remotely forced circulation features passing through our domain and transient adjustments of the local pressure gradients to the changing wind forcing, as well as errors in the HF radar–based velocities themselves and in the tidal or wind-driven velocity extractions described above. A related decomposition of HF radar fields into individual flow components was performed by Ardhuin et al. (2009) to isolate the wind drift and veering angles. While in that paper the authors specifically removed an estimate of the Stokes drift from

the HF radar–measured velocities, due to the weak and almost constant wave conditions present during our drifter experiment, the Stokes drift was not a significant component of the flow here and thus it was not isolated in the decomposition described above.

a. Spatial structure and kinetic energies

The steady summertime mean flow (Fig. 14a) shows a pronounced cyclonic circulation in the northeastern part of the domain centered at around 41.32°N, 70.55°W, which arises as a result of the rectification of the strong semidiurnal tides present (Ganju et al. 2011; Kirincich et al. 2013). A second, much weaker anticyclonic feature is seen in the northwesternmost part of the domain. The flow in the south is dominated by a westward jet, associated
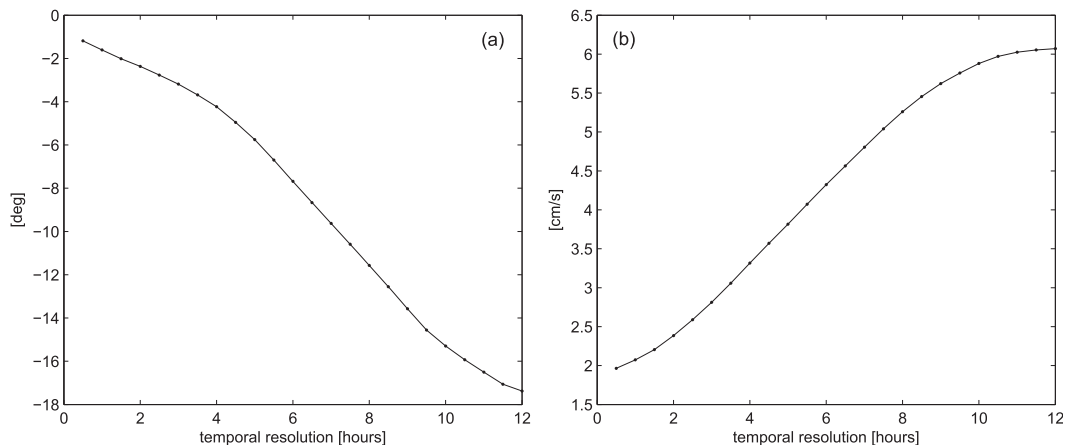
FIG. 11. The domain-averaged mean differences in direction and (a) magnitude between the (b) drifter- and radar-based velocities as a function of the radar temporal resolution.

with a geostrophically balanced along-shelf flow that occurs in summer only (Kirincich et al. 2013). Separating these three features, a hyperbolic stagnation point lies near 41.29°N, 70.62°W. The flow converges to this point in the stable directions from the northwest and southeast and then diverges in the unstable directions to the west and northeast.

It is convenient to think of a sum of the tidal, the locally wind-driven, and the residual flow components as a "perturbation velocity" on top of the steady mean circulation. For each flow component, the spatial patterns of the mean kinetic energy averaged over summer months, defined here as June 1 until September 30, are shown in Fig. 14. Compared to the perturbation velocity, the mean circulation is weak and the associated domain-averaged mean kinetic energy KE_{mean} corresponds to only 5.4% of the spatially and temporally averaged perturbation kinetic energy KE_{pert}. For the summertime period examined, the kinetic energy of the estimated tidal velocities (KE_{tide}) accounts for 54% of the perturbation kinetic energy KE_{pert}. Tidal energy is dominated by the semidiurnal M_2 tide, which is significantly elevated over the shallower northeastern corner of the domain, decaying rapidly to the southwest. The kinetic energy associated with the local wind-driven currents (KE_{wind}) accounts for 23% of KE_{pert}. The kinetic energy of the residual circulation, KE_{res}, is slightly higher (but comparable) to KE_{wind}, representing 28% of KE_{pert} when averaged over the summer. Note that the sum of the kinetic energy fractions given above for each flow component overestimates the kinetic energy of the total velocity due to the separation techniques used and the fact that KE is a squared quantity.

The percentages given above correspond to the summertime averaged values, and thus the relative amount of the total KE in each flow component might deviate from these average values during a particular forcing event. Such is the case during the drifter experiment period, as the start of the experiment was specifically scheduled for the day when the wind was very weak to simplify and speed up the deployment of drifters. Consequently, when averaged over the first 12 h of the experiments, KE_{wind} only accounts for about 9% of KE_{pert}, KE_{res} increases to 37% of KE_{pert}, while the percentage associated with the tidal energy stays roughly the same.

b. Drifter trajectories

Figure 15 shows the simulated trajectories computed using each of the four flow components, that is, the mean, tidal, locally wind-driven, and residual velocities. Not surprisingly, the weak mean and wind-driven currents result in trajectories that are very different from the real drifters. More interesting is the fact that, despite being the strongest, the tidal currents alone also result in very large errors. The simulated trajectories resulting from the residual velocities are qualitatively the most similar to the real trajectories.

To quantify the relative importance of different flow components and their combinations, we constructed plots akin to Fig. 7 but for simulated trajectories computed using the 14 different combinations of one, two, and three flow components (e.g., mean + tides + wind driven). As a consistency check, we have verified that the sum of the four components (which is equal to the total radar-based velocity field) gives the result identical to Fig. 7. Figure 16 reveals that over the 10-h period, simulated trajectories produced using the mean, tidal, and wind-driven currents, and using all combinations that exclude the residual and tidal currents result in much faster separations compared to the total currents case. The residual velocity alone, on the other hand, leads to a fast initial separation (up to about 3 h) but
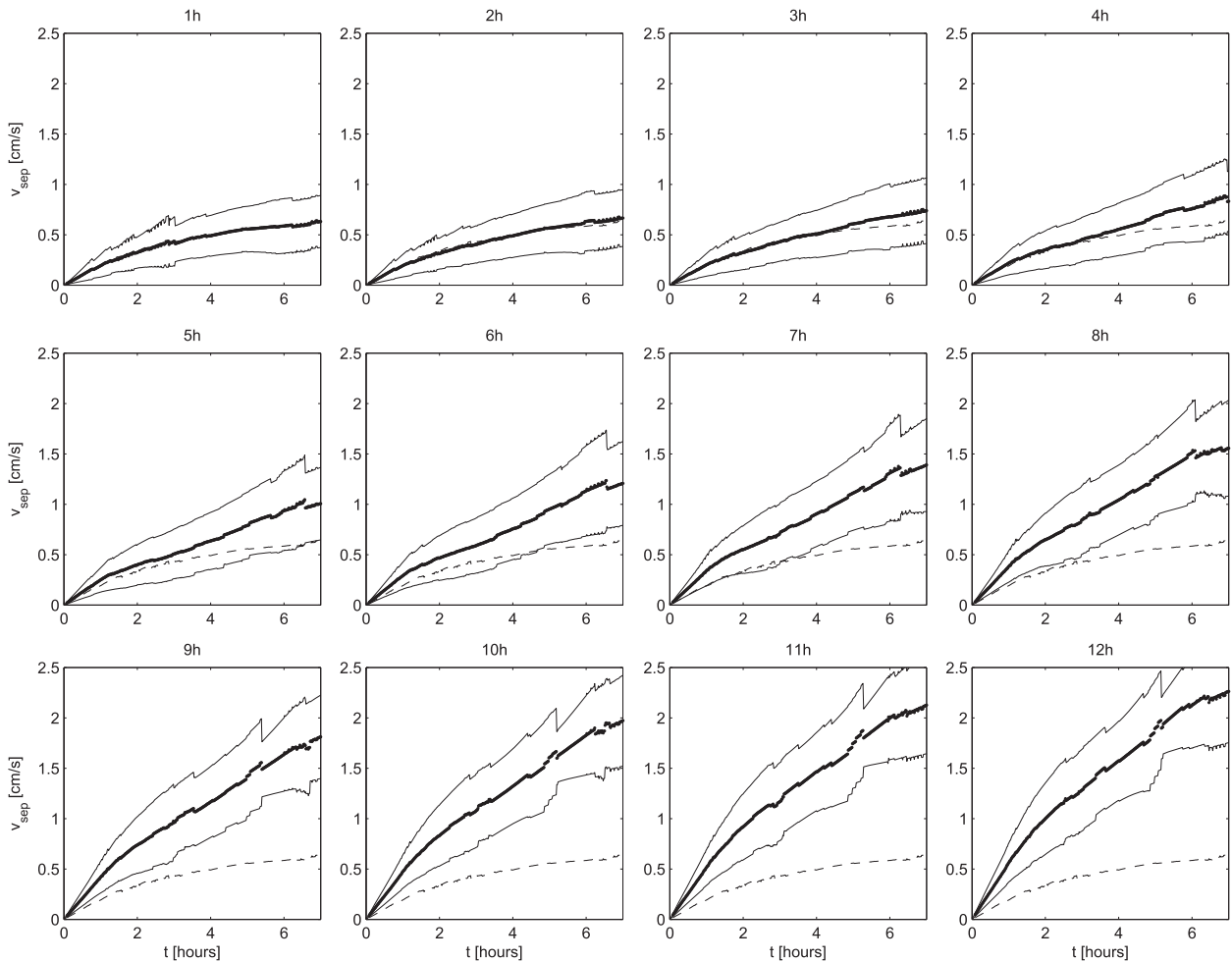
FIG. 12. As in Fig. 7, but for the deteriorated radar velocity fields with various temporal resolution. To aid the comparison, the 30-min-resolution curve is shown as dashed gray in all the subplots.

then the separation slows down and even decreases from 7 to 10 h. This nonmonotonic behavior is present in all subplots that include the residual velocities but exclude tidal velocities (i.e., r, r + w, r + m, and r + m + w). The fast initial separation associated with the residual currents is decreased with the addition of tidal currents (see panel t + r). Note also that the t + r curve is comparable, within the error bars, to the full-velocity curve (dashed).

We thus conclude that, during the time interval considered, the easily "predictable" components of the flow (i.e., the steady, tidal, and wind-driven flows) are unable to sufficiently represent observations. At minimum both the tides and residual currents are needed to give separation velocities that approach that of the full dataset. The implications of this result on the short-time prediction systems currently in place (O'Donnell et al. 2005; Barrick et al. 2012) are discussed next, along with the results in general.

6. Summary and conclusions

The mass drifter release experiment conducted in the coastal ocean south of Martha's Vineyard, Massachusetts, was undertaken to test a new drifter communication system and time-efficient recovery technology, as well as to investigate applicability of dynamical systems techniques to real drifter data. Although designed with the above-mentioned dynamical-systems-oriented goals in mind, the experiment provided a rich dataset to make a detailed comparison between the drifters and the collocated high-resolution HF radar system. Operationally, this pilot field experiment showed that it is possible to efficiently carry out mass drifter experiments (both deployments and recoveries) in a coastal ocean from two coastal vessels using limited manpower (1 scientist + 1 or 2 crew members per vessel). Scientifically, as shown by the results presented above, the release of large numbers of surface drifters allowed us to quantify
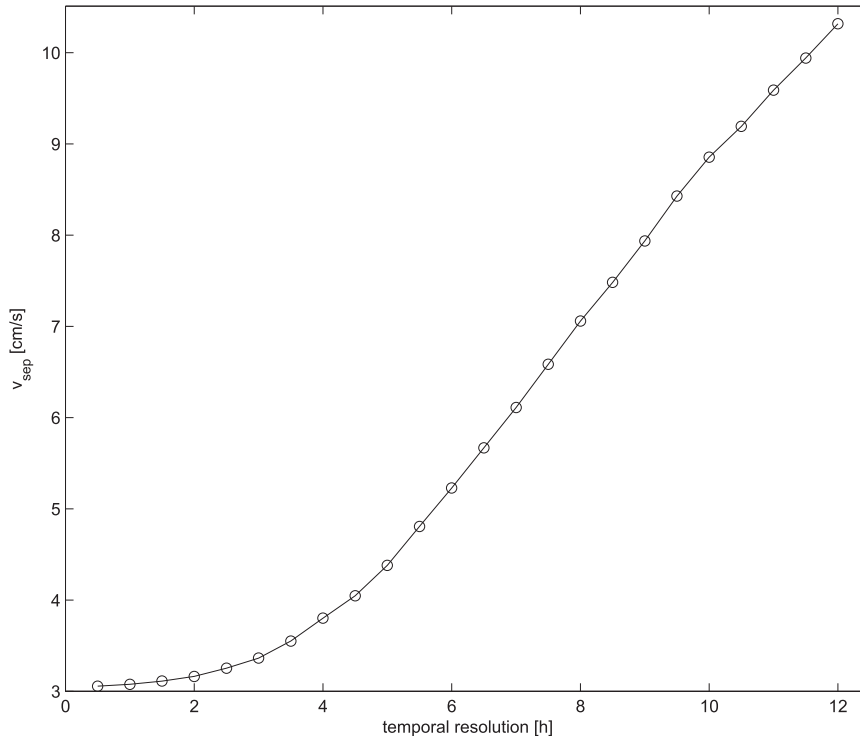
FIG. 13. Separation velocity, averaged over the first 7 h, between the real and simulated drifters as a function of the radar temporal resolution.

the Eulerian and Lagrangian correspondence between drifter data and HF radar data, to investigate the effects of the radar resolution on the resulting velocities and trajectories, and to study the relative importance of different flow components in a coastal ocean. Additional dynamical systems analysis of this dataset is ongoing.

Using the drifter dataset, discrepancies between the drifter and MVCO HF radar–based velocities were found to be among the lowest reported in literature, despite the additional noise inherent in operating the HF radar system at the highest temporal and spatial resolutions possible in the coastal ocean. The careful attention paid to data collection, calibration, and data quality control of the observations made by the MVCO HF radar system, described by Kirincich et al. (2012), were critical to achieving the low error rates. The drifter–radar comparisons revealed that surface velocities estimated from the MVCO HF radar system were unbiased in direction but biased in magnitude with respect to drifter velocities. The radar was found to systematically underestimate drifter-based velocities by about 2 cm s^{-1}, likely as a result of the smoothing effects of the spatial and temporal averaging employed by radar systems. The domain-averaged STD difference between the radar- and drifter-based velocity magnitudes, a

method frequently used to quantify radar accuracy, was found to be about 3.8 cm s^{-1}.

Over the course of the 10 h when the surface drifters were within the HF radar domain, real drifter trajectories separated from simulated trajectories based on HF radar velocities by an average of 1 km. At an equivalent separation speed of 2.8 cm s^{-1}, these separation rates are among the lowest documented for a coastal HF radar system, are consistent with those reported by Molcard et al. (2009), and are only slightly above the published estimates of drifter slippage (1–2 cm s^{-1}) in the coastal ocean (see Ohlmann et al. 2007; Poulain et al. 2009, and references therein).

As described above, because of the large number of drifters deployed and the high temporal and spatial resolutions of the MVCO HF radar system, the results of the experiment were uniquely suited to investigate the effects of the temporal and spatial resolution on the drifter–radar comparisons as well as the effects of the different flow components. By degrading the native high-resolution velocities of the MVCO HF radar system to courser temporal and spatial scales before comparing radar and drifter velocities and trajectories, we investigated the effects of the temporal and spatial resolution of the MVCO HF radar system on its ability to reproduce drifter trajectories. The correspondence between
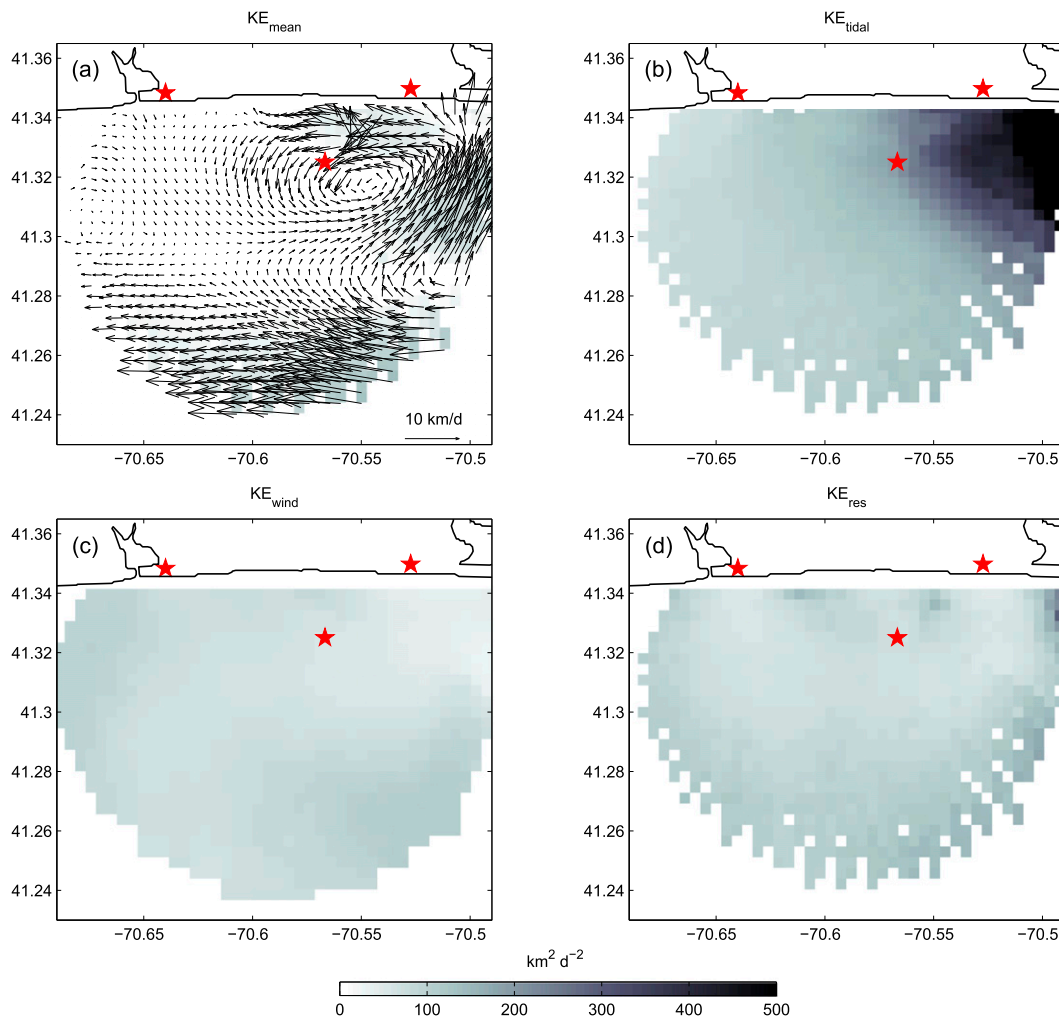
FIG. 14. Time-mean kinetic energy, averaged over summer months (from 1 Jun until 30 Sep) associated with (a) the mean circulation, (b) tidal currents, (c) local-wind-driven currents, and (d) the residual circulation features. Mean circulation is also shown by arrows in panel (a). Domain-averaged standard error of the summertime mean circulation is less than $1\,\mathrm{cm\,s^{-1}}$. Red stars show locations of the three HF radar sites.

simulated and real trajectories at varying resolutions showed that critical spatial and temporal resolutions existed for the dataset considered. Radar observations degraded to length scales longer than about 1.5–2 km or 3 h incurred markedly higher error rates for the differences between simulated and real trajectories. Finally, we have looked at the effects of the different flow components present during the experiment—mean, tidal, locally wind-driven currents, and the residual velocities—and concluded that a minimum combination of the tidal and residual currents was needed to reproduce the trajectories of drifters with minimal degradation.

The MVCO HF radar system is atypical in that it samples temporal and spatial scales considerably higher than many operational HF radar systems worldwide. In contrast, typical long-range coastal HF radar systems

have averaging periods of 3–6 h and spatial resolutions of 6–7 km, although the spatial averaging radius typically used for estimating vector velocities at each grid point is generally 20–25 km. Thus, the investigation of the effect of spatial and temporal resolutions on the accuracy of simulated trajectories is, to our knowledge, the first of its kind and has potentially broad implications. Based on the results shown above, higher resolutions generally give more accurate results, but the change in the slope of the curves shown in Figs. 10 and 13 at roughly 1.5–2 km and 3 h points toward the existence of the critical spatial and temporal scales of flow in the study area below which the performance of the radar drops dramatically. These critical scales should be viewed as properties of the underlying physical flow that need to be resolved to reliably reproduce real drifter tracks.
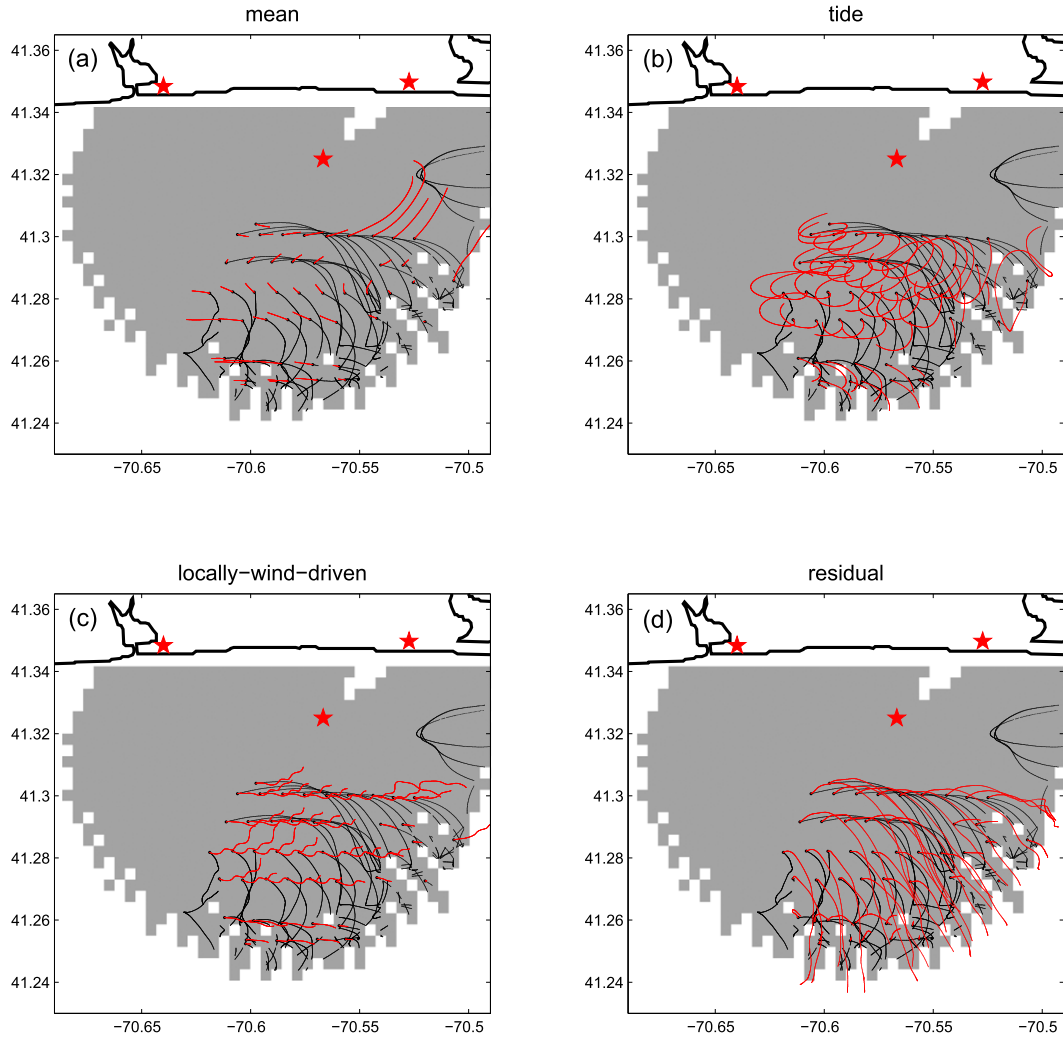
FIG. 15. Real (black) and simulated (red) trajectories computed using each of the four flow components: (a) mean, (b) tidal, (c) locally wind-driven, and (d) residual velocities. Red stars show locations of the three HF radar sites.

While the exact magnitude of the critical space and time scales found here are likely specific to the study area, the existence of critical scales could be expected in other locations, though likely normalized by the distance to the coastline.

Based on the results presented here, we can offer a number of suggestions for ways to reduce the differences between radar-based and real drifter trajectories for the more typical medium- and long-range coastal HF radar systems in this location as well as others. For this purpose we have looked at the combined effect of simultaneously degrading the temporal and spatial resolution (dashed and dotted curves, respectively, in Fig. 10). Based on our results, for a system operating at a coarse spatiotemporal resolution of 6 h and 3.5 km, improving the temporal resolution has the greater effect than improving the spatial resolution. As illustrated in

Fig. 10 for this particular example, changing the temporal resolution to from 6 to 3 h would result in the reduction of separation velocities from >6 to 4.6 cm s^{-1}, whereas changing the spatial resolution to 400 m would only drop the separation velocities to 5.2 cm s^{-1}. On the other hand, for a system operating at 3 h and 3.5-km resolution, we observe a stronger response to the improved spatial resolution rather than temporal resolution. Comparison between the dashed and solid curves in Fig. 10 illustrates that as the spatial resolution is improved to 400 m, the separation velocity drops from 4.6 to 3.4 cm s^{-1}, whereas improving the temporal resolution to 30 min only yields to a decrease in v_{sep} from 4.6 to 4.2 cm s^{-1}.

Generally speaking, improving the spatial resolution of an HF radar system can be difficult. While careful processing, antenna calibration, and weighted-averaging methods might allow finer azimuthal resolution to be
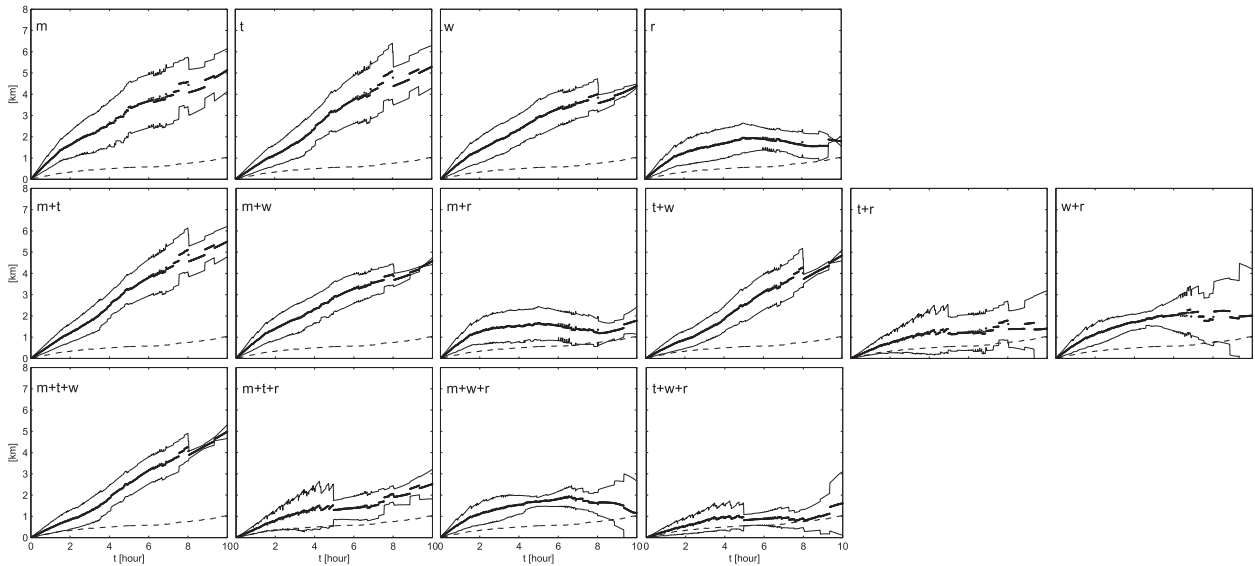
FIG. 16. As in Fig. 7, but for simulated trajectories computed using the 14 different combinations of one, two, and three flow components. Letters in the left corner of each plot mark the corresponding combination: "m" denotes mean, "t" denotes tides, "w" denotes locally wind-driven currents, and "r" is short for residual currents. Dashed curve shows the separation curve for the total radar-based velocities.

employed without significant degradation of the signal quality, the radial spatial resolution for the existing low- (4–5 MHz) and mid- (11–13 and 24–26 MHz) frequency systems is a function of bandwidth, which is tightly controlled and limited to a few narrow bands by law. However, the new allocated bands and total bandwidths for HF radar–based surface currents recently negotiated during the World Radiocommunication Conference 2012 (WRC-12) offer some hope, as a sizable bandwidth of 50 kHz now exists in the 4.4-MHz range. Thus, we suggest that small-frequency, $O(100\,\text{Hz})$, offsets and GPS-based timings can be utilized to allow a large number of 4.4-MHz systems to share this bandwidth, improving the range resolution of these systems to 3 km. Based on our results, with careful attention to data processing methods, this change has the potential to decrease trajectory prediction errors of the long-range systems to values as small as 3–4 km day^{-1}. As a point of comparison, trajectory prediction errors of 7–10 km day^{-1} were recently documented for long-range HF radar systems using standard methods and resolutions by Ullman et al. (2006). Thus, changes in sampling and resolution could likely cut trajectory prediction errors in half. We note, however, that our analysis might be specific to our geographical region and time interval, so our conclusions (and suggestions) might not hold for other coastal regions.

Additional improvements to the radar-based trajectory predictions could be achieved by correcting the radar velocity magnitudes for the mean bias. For the MVCO

radar system, adjusting the radar velocity magnitudes to account for the $2\,\text{cm s}^{-1}$ mean underestimate led to a roughly 18% decrease in the separation velocity between the real and simulated trajectory pairs, which decreased from 2.8 to 2.3 cm s^{-1}. We expect that for typical long-range systems, the mean velocity underestimate (bias) could be even more severe, and thus the simple velocity adjustment could lead to even more significant improvements in the radar performance.

The importance of the residual velocities here—which, by definition, cannot be predicted from local measurements alone—is potentially important for the short-time prediction systems used for search and rescue planning operations (O'Donnell et al. 2005; Barrick et al. 2012), as it suggests that a combination of the predicted tidal and locally wind-driven currents, commonly proposed as a way to estimate or forecast future currents, is not always likely to significantly improve forecast estimates. While a similar conclusion was reached by (O'Donnell et al. 2005), they suggested that the reason for this was the HF radar velocities themselves. Based on the results shown here, this is only partially true. While further improvements in HF radar estimates of velocities can be obtained with additional calibrations and advanced data quality controls and data processing as suggested above, the role of the nonlocal and thus unknown residual component of the circulation cannot be discounted. Thus, while improved HF radar velocities are possible and necessary, improved long-term trajectory estimation will likely require the inclusion of a fully coupled, assimilative,

regional numerical model that is guided by the surface current observations.

REFERENCES

Ardhuin, F., L. Marie, N. Rascle, P. Forget, and A. Roland, 2009: Observation and estimation of Lagrangian, Stokes, and Eulerian currents induced by wind and waves at the sea surface. *J. Phys. Oceanogr.,* **39,** 2820–2838, doi:10.1175/2009JPO4169.1.

Barrick, D. E., and B. J. Lipa, 1997: Evolution of bearing determination in HF current mapping radars. *Oceanography,* **10,** 72–75, doi:10.5670/oceanog.1997.27.

——, M. Evans, and B. Weber, 1977: Ocean surface currents mapped by radar. *Science,* **198,** 138–144, doi:10.1126/science.198.4313.138.

——, V. Fernandez, M. I. Ferrer, C. Whelan, and O. Breivik, 2012: A short-term predictive system for surface currents from a rapidly deployed coastal HF radar network. *Ocean Dyn.,* 725–740, doi:10.1007/s10236-012-0521-0.

Chen, C., and Coauthors, 2014: Process modeling studies of physical mechanisms of the formation of an anticyclonic eddy in the central Red Sea. *J. Geophys. Res. Oceans,* doi:10.1002/2013JC009351, in press.

Crombie, D., 1955: Doppler spectrum of the sea echo at 13.56 Mc./s. *Nature,* **175,** 681–682, doi:10.1038/175681a0.

Edson, J. B., and Coauthors, 2007: The coupled boundary layers and air–sea transfer experiment in low winds. *Bull. Amer. Meteor. Soc.,* **88,** 341–356, doi:10.1175/BAMS-88-3-341.

Emery, B., L. Washburn, and J. Harlan, 2004: Evaluating radial current measurements from CODAR high-frequency radars with moored current meters. *J. Atmos. Oceanic Technol.,* **21,** 1259–1271, doi:10.1175/1520-0426(2004)021<1259:ERCMFC>2.0.CO;2.

Fewings, M., S. Lentz, and J. Fredericks, 2008: Observations of cross-shelf flow driven by cross-shelf winds on the inner continental shelf. *J. Phys. Oceanogr.,* **38,** 2358–2378, doi:10.1175/2008JPO3990.1.

Ganju, N., S. Lentz, A. Kirincich, and J. Farrar, 2011: Complex mean circulation over the inner shelf south of Martha's Vineyard revealed by observations and a high-resolution model. *J. Geophys. Res.,* **116,** C10036, doi:10.1029/2011JC007035.

Gerbi, G., J. Trowbridge, J. Edson, A. Plueddemann, E. Terray, and J. Fredericks, 2008: Measurements of momentum and heat transfer across the air–sea interface. *J. Phys. Oceanogr.,* **38,** 1054–1072, doi:10.1175/2007JPO3739.1.

Haller, G., 2002: Lagrangian coherent structures from approximate velocity data. *Phys. Fluids,* **14,** 1851–1861, doi:10.1063/1.1477449.

He, R., and J. Wilkin, 2006: Barotropic tides on the southeast New England shelf: A view from a hybrid data assimilative modeling approach. *J. Geophys. Res.,* **111,** C08002, doi:10.1029/2005JC003254.

IOOS, 2011: IOOS in action: Deepwater Horizon oil spill response. NOAA, 2 pp. [Available online at http://www.ioos.noaa.gov/library/deepwater_horizon_051911.pdf.]

Kirincich, A., T. de Paolo, and E. Terrill, 2012: Improving HF radar estimates of surface currents using signal quality metrics, with application to the MVCO high-resolution radar system. *J. Atmos. Oceanic Technol.,* **29,** 1377–1390, doi:10.1175/JTECH-D-11-00160.1.

——, S. Lentz, J. Farrar, and N. Ganju, 2013: The spatial structure of tidal and mean circulation over the inner shelf south of Martha's Vineyard, Massachusetts. *J. Phys. Oceanogr.,* **43,** 1940–1958, doi:10.1175/JPO-D-13-020.1.

Kohut, J., S. Glenn, and R. Chant, 2004: Seasonal current variability on the New Jersey inner shelf. *J. Geophys. Res.,* **109,** C07S07, doi:10.1029/2003JC001963.

——, H. Roarty, and S. Glenn, 2006: Characterizing observed environmental variability with HF Doppler radar surface current mappers and acoustic Doppler current profilers: Environmental variability in the coastal ocean. *IEEE J. Oceanic Eng.,* **31,** 876–884, doi:10.1109/JOE.2006.886095.

Kosro, P. M., 2005: On the spatial structure of coastal circulation off Newport, Oregon, during spring and summer 2001 in a region of varying shelf width. *J. Geophys. Res.,* **110,** C10S06, doi:10.1029/2004JC002769.

Large, W., and S. Pond, 1981: Open ocean momentum flux measurements in moderate to strong winds. *J. Phys. Oceanogr.,* **11,** 324–336, doi:10.1175/1520-0485(1981)011<0324:OOMFMI>2.0.CO;2.

Lekien, F., C. Coulliette, A. J. Mariano, E. H. Ryan, L. K. Shay, G. Haller, and J. E. Marsden, 2005: Pollution release tied to invariant manifolds: A case study for the coast of Florida. *Physica D,* **210,** 1–20, doi:10.1016/j.physd.2005.06.023.

Lentz, S., 2008: Observations and a model of the mean circulation over the Middle Atlantic Bight continental shelf. *J. Phys. Oceanogr.,* **38,** 1203–1221, doi:10.1175/2007JPO3768.1.

——, M. Fewings, P. Howd, J. Fredericks, and K. Hathaway, 2008: Observations and a model of undertow over the inner continental shelf. *J. Phys. Oceanogr.,* **38,** 2341–2357, doi:10.1175/2008JPO3986.1.

Lumpkin, R., A.-M. Treguier, and K. Speer, 2002: Lagrangian eddy scales in the northern Atlantic Ocean. *J. Phys. Oceanogr.,* **32,** 2425–2440, doi:10.1175/1520-0485-32.9.2425.

Molcard, A., P. Poulain, P. Forget, A. Griffa, Y. Barbin, J. Gaggelli, J. C. De Maistre, and M. Rixen, 2009: Comparison between VHF radar observations and data from drifter clusters in the Gulf of La Spezia (Mediterranean Sea). *J. Mar. Syst.,* **78,** S79–S89, doi:10.1016/j.jmarsys.2009.01.012.

O'Donnell, J., and Coauthors, 2005: Integration of Coastal Ocean Dynamics Application Radar (CODAR) and Short-Term Predictive System (STPS) surface current estimates into the Search and Rescue Optimal Planning System (SAROPS). U.S. Coast Guard Final Rep. CG-D-01-2006, 163 pp. [Available online at http://www.dtic.mil/get-tr-doc/pdf?AD=ADA444766.]

Ohlmann, C., P. White, L. Washburn, E. Terrill, B. Emery, and M. Otero, 2007: Interpretation of coastal HF radar–derived surface currents with high-resolution drifter data. *J. Atmos. Oceanic Technol.,* **24,** 666–680, doi:10.1175/JTECH1998.1.

Olascoaga, M. J., I. I. Rypina, M. G. Brown, F. J. Beron-Vera, H. Kocak, L. E. Brand, G. R. Halliwell, and L. K. Shay, 2006: Persistent transport barrier on the west Florida shelf. *Geophys. Res. Lett.,* **33,** L22603, doi:10.1029/2006GL027800.

Paduan, J., and H. Graber, 1997: Introduction to high-frequency radar: Reality and myth. *Oceanography,* **10,** 36–39, doi:10.5670/oceanog.1997.18.

——, K. Kim, M. Cook, and F. Chavez, 2006: Calibration and validation of direction-finding high frequency radar ocean surface current observations. *IEEE J. Oceanic Eng.,* **31,** 862–875, doi:10.1109/JOE.2006.886195.

Pawlowicz, R., B. Beardsley, and S. Lentz, 2002: Classical tidal harmonic analysis including error estimates in MATLAB using T_TIDE. *Comput. Geosci.,* **28,** 929–937, doi:10.1016/S0098-3004(02)00013-4.

Poulain, P.-M., R. Gerin, and E. Mauri, 2009: Wind effects on drogued and undrogued drifters in the eastern Mediterranean. *J. Phys. Oceanogr.,* **26,** 1144–1156, doi:10.1175/2008JTECHO618.1.

Ramp, S., J. Paduan, I. Shulman, J. Kindle, F. Bahr, and F. Chavez, 2005: Observations of upwelling and relaxation events in the northern Monterey Bay during August 2000. *J. Geophys. Res.,* **110,** C07013, doi:10.1029/2004JC002538.

Rypina, I. I., L. J. Pratt, J. Pullen, J. Levin, and A. Gordon, 2010: Chaotic advection in an archipelago. *J. Phys. Oceanogr.,* **40,** 1988–2006, doi:10.1175/2010JPO4336.1.

——, S. E. Scott, L. J. Pratt, and M. G. Brown, 2011: Investigating the connection between complexity of isolated trajectories and Lagrangian coherent structures. *Nonlinear Processes Geophys.,* **18,** 977–987, doi:10.5194/npg-18-977-2011, 2011.

Samelson, R. M., and S. Wiggins, 2006: *Lagrangian Transport in Geophysical Jets and Waves: The Dynamical Systems Approach.* Interdisciplinary Applied Mathematics, Vol. 31, Springer-Verlag, 147 pp.

Schmidt, R., 1986: Multiple emitter location and signal parameter estimation. *IEEE Trans. Antennas Propag.,* **34,** 276–280, doi:10.1109/TAP.1986.1143830.

Shadden, S. C., F. Lekien, J. D. Paduan, F. P. Chavez, and J. E. Marsden, 2009: The correlation between surface drifters and coherent structures based on high-frequency radar data in Monterey Bay. *Deep-Sea Res. II,* **56,** 161–172, doi:10.1016/j.dsr2.2008.08.008.

Shearman, R. K., and S. J. Lentz, 2004: Observations of tidal variability on the New England shelf. *J. Geophys. Res.,* **109,** C06010, doi:10.1029/2003JC001972.

Stewart, R., and J. Joy, 1974: HF radio measurements of surface currents. *Deep-Sea Res.,* **21,** 1039–1049, doi:10.1016/0011-7471(74)90066-7.

Ullman, D., and D. Codiga, 2004: Seasonal variation of a coastal jet in the Long Island Sound outflow region based on HF radar and Doppler current observations. *J. Geophys. Res.,* **109,** C07S06, doi:10.1029/2002JC001660.

——, J. O'Donnell, J. Kohut, T. Fake, and A. Allen, 2006: Trajectory prediction using HF radar surface currents: Monte Carlo simulations of prediction uncertainties. *J. Geophys. Res.,* **111,** C12005, doi:10.1029/2006JC003715.

Wilkin, J., 2006: The summertime heat budget and circulation of southeast New England shelf waters. *J. Phys. Oceanogr.,* **36,** 1997–2011, doi:10.1175/JPO2968.1.